Plasma Chem Plasma Process (2016) 36:941–972
DOI 10.1007/s11090-016-9721-6

ORIGINAL PAPER

Synthesis of Silicon Nanoparticles in Nonthermal Capacitively-Coupled Flowing Plasmas: Processes and Transport

Romain Le Picard[1] · Aram H. Markosyan[2] · David H. Porter[3] · Steven L. Girshick[1] · Mark J. Kushner[2]

Received: 29 March 2016 / Accepted: 16 May 2016 / Published online: 27 May 2016

Abstract Control of the size and material properties of silicon nanoparticles plays a critical role in optimizing applications using those nanoparticles, such as photovoltaics and biomedical devices. While synthesis of silicon nanoparticles in low temperature plasmas has many attractive features, the basic mechanisms leading to formation of nanoparticles in these plasmas are poorly understood. A two-dimensional numerical model for synthesis of silicon nanoparticles (<5 nm in diameter) in radio frequency (RF) discharges was developed and used to investigate mechanisms for particle growth for Ar/He/SiH_4 gas mixtures. Algorithms for the kinetics of nanoparticle formation were self-consistently embedded into a plasma hydrodynamics simulation to account for nucleation, growth, charging, and transport of nanoparticles. We found that with RF excitation in narrow tubes at pressures of a few Torr, the electric field does not fully confine charged nanoparticles in the axial direction, which then results in a finite residence time of particles in the plasma. We found that because of the high neutral nanoparticle density, coagulation plays a significant role in

✉ Romain Le Picard
rlepicar@umn.edu

Aram H. Markosyan
armarkos@umich.edu

David H. Porter
dhp@umn.edu

Steven L. Girshick
slg@umn.edu

Mark J. Kushner
mjkush@umich.edu

[1] Department of Mechanical Engineering, University of Minnesota, 111 Church Street SE, Minneapolis, MN 55455, USA

[2] Electrical Engineering and Computer Science Department, University of Michigan, 1301 Beal Ave., Ann Arbor, MI 48109-2122, USA

[3] Minnesota Supercomputing Institute, University of Minnesota, 117 Pleasant St. SE, Minneapolis, MN 55455, USA

growth. The model predicts the possibility of synthesizing crystalline silicon nanoparticles under these conditions. Trends in the growth of nanoparticles as a function of power are discussed.

Keywords Silicon nanoparticle synthesis · Plasma modeling · Nanoparticle charging

Introduction

The formation and growth of silicon nanoparticles (diameter < 10 nm) in plasmas have been extensively investigated since the early 1990s due to many potential applications in light emission devices, electronics, sensors, catalysis, photovoltaics, biomedical imaging, cell biology, medicine and renewable energy [1–7]. While a variety of nanoparticle materials have been explored, there is particular interest in Si nanoparticles due to an already existing technological knowledge base for Si-based materials. Si nanoparticle synthesis in the gas phase is a well-established technique. However, nanoparticle agglomeration makes the size of the nanoparticles, or their monodisperse nature, difficult to control [8, 9]. Nanoparticle synthesis using nonthermal plasmas has unique features in terms of cleanliness, and control of size and crystallinity [7, 10]. For example, the charging of nanoparticles in nonthermal plasmas tends to reduce the likelihood of mutual coagulation and so produces narrower size distributions. In parallel-plate systems, negatively charged nanoparticles can be confined by electric fields in the plasma, which increases their residence time and promotes growth. Nonthermal plasmas can be sustained at low and atmospheric pressures which extends the operational window for nanoparticle synthesis [11–14].

Nonthermal plasmas can also selectively heat nanoparticles significantly above the gas temperature which in turn aids in their crystallization. The crystallization temperature of amorphous silicon nanoparticles in the range of 4–10 nm in size is about 700–1200 K [15], which is typically much higher than the gas temperature in nonthermal plasmas. Monte Carlo models have shown that the nanoparticle temperature in these plasmas can fluctuate above the crystallization temperature due to hydrogen reactions and electron–ion recombination on the surface [16].

In typical low-pressure plasma conditions, the formation (nucleation) of nanoparticles occurs through a polymerization chain of reactions producing small clusters (tens of silicon atoms). The clusters grow through coagulation, where two nanoparticles collide to form a larger particle, and surface growth due to the deposition of silicon hydride radicals on nanoparticle surfaces. Nanoparticle formation and growth mechanisms have been experimentally investigated by Boufendi and Bouchoule [17]. They found that nanoparticle formation in argon-silane discharges occurred in three steps (1) rapid nucleation, (2) coagulation and reduction of total nanoparticle density, followed by (3) surface deposition of radicals on nanoparticle surfaces while the nanoparticle density remains nearly constant. There are limited experimental techniques that provide the fundamental parameters needed to determine the growth mechanisms of nanoparticles in non-thermal plasmas. The time evolution of particle size and concentration can be found from electrical measurements [18] or laser light scattering [17]. The consequences of nanoparticles on plasma properties have been investigated by Langmuir probe measurements of electron energy distributions [19–22]. It is difficult to directly measure the growth of particles following their

nucleation. To date, there are few direct experimental measurements of chemical reaction pathways, the spatial distribution of plasma potential, nanoparticle charge fluctuations, and other processes that may influence particle growth. This is particularly true of measuring size-resolved, spatial distributions of nanoparticles in the plasma, measurements that challenge laser light scattering. This situation motivates use of computer modeling to help understand the mechanisms leading to nanoparticle synthesis.

As mentioned, silicon nanoparticles in plasmas are thought to nucleate through a polymerization chain in which small radicals are added to a larger growing silicon hydride cluster. Detailed plasma chemistry models have been developed whose results suggest that anionic pathways (that is, reactions involving negative ions) are responsible for particle nucleation due to the trapping of negatively charged particles in electropositive plasmas, which causes them to have a longer residence time than neutral and positive species in parallel-plate systems [23, 24]. Recently, ab initio calculations were used to understand the mechanisms of nucleation reactions at a molecular level [25]. Due to the larger rate coefficients of ion–molecule reactions compared to neutral–neutral reactions, and the trapping of negative particles by the electric field in the plasma, nanoparticle transport and growth are strongly coupled to nanoparticle charging. Under typical low-pressure plasma conditions, nanoparticles are mostly negatively charged. However, for particles that are only a few nanometers or less in diameter, the stochastic nature of charging results in charge distributions that strongly affect nanoparticle growth and transport [26–28].

Although the kinetics of nanoparticle growth in plasmas involves additional processes compared to non-plasma systems, the basic techniques of investigating nucleation and growth developed in the aerosol community still apply. One such technique is the sectional representation of the particle size distribution. The range of nanoparticle sizes is divided into smaller individual ranges called sections. Each section corresponds to a range of sizes represented by an average diameter, surface area and volume.

Recently, a one-dimensional self-consistent model of a parallel plate capacitively-coupled radio frequency (RF) plasma was developed using a sectional model to investigate nanoparticle nucleation, transport, charging, and growth [29, 30]. For each size in the sectional model, a distribution of particle charge was determined based on local plasma properties. These studies found that coagulation can make a significant contribution to nanoparticle growth due to the high collision rate between negatively-charged and neutral nanoparticles, enhanced by the occurrence of image potentials in the neutral particle [31].

To provide insight into the fundamental processes and mechanisms of nanoparticle synthesis in low-pressure, nonthermal plasmas, in the present work, nanoparticle formation kinetics based on a sectional model were embedded into a two-dimensional plasma hydrodynamics model. The model was applied to the investigation of Si particle synthesis in a capacitively-coupled RF plasma sustained in Ar/He/SiH_4 mixtures flowing through a narrow quartz tube. The geometry is based on the experiments of Kortshagen and coworkers [11, 32, 33]. We found that nanoparticles, which are mostly negatively charged, are trapped radially in the plasma but not in the axial direction. Therefore, their size can be tuned by varying the background gas flow, as proposed experimentally. Due to the high neutral nanoparticle density, coagulation plays a significant role in particle growth.

The model used in this investigation is described in the second section, followed by a discussion of computational challenges in the third section. Base case results for growth mechanisms, charging, and transport of nanoparticles are presented in the fourth section. Temperature fluctuations of the nanoparticles are described in the fifth section, and scaling with power is discussed in the sixth section. Concluding remarks are in the seventh section.

Description of the Model

In this section, we describe the model we developed to simulate a capacitively-coupled RF plasma reactor for the synthesis of silicon nanoparticles. The basic model consists of a two-dimensional plasma-hydrodynamics simulation into which algorithms for particle nucleation, growth, transport and charging have been embedded in a self-consistent manner. Particle growth is described by a sectional model.

The basic plasma model into which the sectional model was embedded is the two-dimensional computational framework Hybrid Plasma Equipment Model (HPEM) [34]. The HPEM combines different modules that address different physical phenomena in low-temperature plasmas. The electron energy transport module (EETM) and the fluid kinetics-Poisson module (FKPM) were used in this work. Continuity, momentum, and energy equations are separately solved for heavy species in the FKPM with collisional exchange terms for transfer of momentum and energy between species. Electron fluxes are provided by a drift–diffusion approximation. Diffusion and mobility coefficients, as well as all electron impact rate coefficients, are derived from electron energy distributions (EEDs) obtained by solving Boltzmann's equation using a two-term approximation. Poisson's equation is solved for the electric potential. A full description of the HPEM is contained in Ref. [34].

An Aerosol Sectional Module (ASM) that produces both particle size and charge distributions was developed and integrated into HPEM. The ASM is based on the work of Warthesen and Girshick [29] in which a one-dimensional self-consistent plasma transport simulation was coupled to nanoparticle transport and growth algorithms. This model was further improved by Agarwal and Girshick [30]. The experiments that motivated the present work produced nanoparticles of 1–5 nm in diameter, which correspond to about 30–3000 silicon atoms per particle, assuming the mass density of bulk silicon ($\rho = 2.33$ g cm^{-3}). For typical plasma conditions, silicon nanoparticles of these sizes may charge up to 5q (q is the electron charge) [28]. As a result, there is a large number of possible discrete size-charge combinations and it would not be computationally tractable to solve continuity, momentum and energy equations for every possible nanoparticle species having a unique charge and number of Si atoms. Sectional modeling provides a compromise between accuracy and computational efficiency [35].

In a sectional model, each section corresponds to a range of particle sizes, which is represented by an average size, volume, and surface area of the particle. The size of each section size logarithmically varies, so that the smaller volume of each section depends on the previous section as

$$v_j = a v_{j-1}, \tag{1}$$

where is v_{j-1} is the volume of the smaller section $j - 1$ and a is the spacing factor of the sectional model. The spacing factor is critical for accurate simulations—it needs to be small enough to avoid numerical diffusion [36], and large enough to effectively reduce the number of sections and so reduce the computational burden. Each section is composed of section-averaged particles having different charge states so that a particle charge distribution can be calculated. With this representation, the number of sets of continuity, momentum and energy equations solved for the nanoparticles represented by sections is $N_p = \sum_j s_j$, where the sum is over all sections and s_j is the number of charge states in section j.

The number of charge states for a particular section is selected based on its charge limit—the maximum number of electrons that can coexist on a single particle [28]. Assuming bare silicon nanoparticles, electron field emission is the primary mechanism which limits charges for particles smaller than 10 nm [37]. Particles up to 2.4 nm in diameter have a charge limit equal to 1. For the experimental conditions investigated in this work, the electron temperature is greater than 3 eV. By estimating electron and ion currents to particles, we expect charged nanoparticles to be mostly negative. Stochastic charging is expected to result in many particles being neutral, while only a small fraction of nanoparticles is expected to be positively charged. Therefore, we have neglected positively-charged nanoparticles in this work. Each section represents either neutral or negatively-charged nanoparticles, with the negative charge ranging from unity up to the charge limit corresponding to the nanoparticle size in that section. Since nanoparticles produced here are mostly smaller than 3 nm, there are mostly two charge states per section—neutral and 1 negative charge.

The ASM is embedded in the HPEM in the following manner. The HPEM is a multi-fluid model, which means that separate mass, momentum and energy equations are solved for each heavy species. Collisional exchange terms for momentum and energy couple the momentum and temperature of each species with other species. These equations for species i, integrated in time simultaneously with Poisson's equations in a semi-implicit manner, are

$$\frac{\partial N_i}{\partial t} = -\nabla \cdot \vec{\phi}_i + S_i \tag{2}$$

$$\frac{\partial \vec{\phi}_i}{\partial t} = -\frac{1}{m_i}\nabla(N_i k_B T_i) - \nabla \cdot (N_i \vec{v}_i \vec{v}_i) + \frac{q_i}{m_i} N_i \vec{E} - \nabla \cdot \bar{\bar{\mu}}_i - \sum_j \frac{m_j}{m_i + m_j} N_i N_j (\bar{v}_i - \bar{v}_j) v_{ij} \tag{3}$$

$$\begin{aligned} \frac{\partial (N_i c_i T_i)}{\partial t} = {} & \nabla \cdot k \nabla T_i - P_i \nabla \cdot \vec{v}_i - \nabla \cdot (N_i \vec{v}_i \varepsilon_i) + \frac{N_i q_i^2}{m_i v_i} E_s^2 \\ & + \sum_j 3 \frac{m_{ij}}{m_i + m_j} N_i N_j v_{ij} k_B (T_j - T_i) - \sum_k R_k f_{ik} \Delta H_k \end{aligned} \tag{4}$$

where N_i, T_i, m_i, $\vec{\phi}_i$, and S_i are the density, temperature, mass, flux, and source for species i, and $\vec{E}_s$ is the electrostatic field produced by solving Poisson's equation. $\bar{v}_i$ is velocity, $\bar{\bar{\mu}}_i$ is the viscosity tensor (used only for neutral species), v_{ij} is the collision frequency between species i and species j, and ε_i is the internal energy. k_B is Boltzmann's constant, c_i is the heat capacity, κ_i is the thermal conductivity, q_i is the charge, and P_i is the partial pressure. The last term in Eq. (4) is a sum over reactions which accounts for exo- or endothermic processes where R_k is the source term ($\mathrm{cm}^{-3}\ \mathrm{s}^{-1}$) for reaction k having change in enthalpy ΔH_k and f_{ik} is the fraction of that enthalpy that is partitioned to species i. In principle, the nanoparticles are included in HPEM by adding N_P sets of continuity, momentum and energy equations to the hierarchy for charged and neutral particle transport. This was accomplished in the following manner.

Nanoparticles nucleate in the first section and grow to higher sections by coagulation and surface growth. Coagulation is the collision between nanoparticles from different (or the same) sections to make larger particles. Surface growth is the deposition of silicon hydride radicals on the nanoparticle surface. The continuity equation for a unique charge state of a given section is

$$\frac{dN_{j,k}}{dt} = -\nabla \cdot \vec{\phi}_{j,k} + S_{nuc} + S_{coag} + S_{growth} + S_{charging}, \quad (5)$$

where j and k refer to section and charge respectively, $N_{j,k}$ is the nanoparticle density, $\vec{\phi}_{j,k}$ is the flux, and the source terms S are for nucleation, coagulation, surface growth, and charging. Summaries of each source term in Eq. (5) are given below, while detailed descriptions can be found in Refs. [29, 30].

Due to their small size, gravity is not important in the transport of nanoparticles whereas gravity can be important to the transport of particles exceeding a few microns in diameter [38]. The fluid and ion drag terms that are included in modeling the transport of macroscopic particles are naturally accounted for in the exchange terms of Eqs. (3) and (4).

The species included in the model are listed in Table 1. We equate the nucleation rate to the rate of formation of small clusters of some specified size. Under similar plasma conditions, Bhandarkar et al. [23] concluded that clusters are formed by a polymerization chain starting from the anionic silylene ($Si_2H_4^-$) and silyl ($Si_2H_5^-$) species. The

Table 1 Species in the plasma chemistry model

Argon species	
Ar (3*s*)	Ar^+
Ar ($1s_5$)	Ar_2^+
Ar ($1s_4$)	
Ar ($1s_3$)	
Ar ($1s_2$)	
Ar (4*p*)	
Ar (4*d*)	
Ar_2*	
Helium species	
He	
He*	
He^+	
Hydrogen species	
H	H^-
H_2	H_2^+
H_2*	H^+
H*	
Silicon hydride species	
Si	SiH^-
Si_2	SiH_2^-
SiH	SiH_3^-
SiH_2	$Si_2H_3^-$
SiH_3	$Si_2H_4B^-$
SiH_4	$Si_2H_5^-$
Si_2H_2	SiH_3^+
Si_2H_3	
Si_2H_4B (B for silylene)	
Si_2H_5	
Si_2H_6	

dominance of the anionic pathways in the formation of clusters is due to the trapping of negative species, as well as to the faster kinetics of ion-neutral reactions compared to reactions between neutral molecules. As particles grow to hundreds of nm to microns in size, ion and fluid drag forces can dominate over electrostatic forces which would otherwise drift negative particles to the maximum in the plasma potential. Under these conditions, ion drag forces from positive ions can move negative particles to the edges of sheaths at boundaries where they are trapped. If the ion flux is high enough, ion drag can push negative particles through the sheaths to surfaces. In the same manner, fluid drag forces on particles of a few microns can entrain the particles in the convective flow out of the reactor even if they are charged [13]. Small negative nanoparticles will likely be accelerated toward the centerline of the reactor, where the time-averaged plasma potential is most positive, while neutral and positive species can diffuse or drift to the walls. Therefore the negative species will be concentrated around the centerline, again making an anionic pathway the likely route for cluster growth. The nucleation rate is taken as the sum of the rates of reactions that involve $Si_2H_4^-$ or $Si_2H_5^-$ species as a reactant and that add one Si atom to the anion cluster—11 reactions in our mechanism, listed in Table 2:

$$S_{nuc} = \sum_n R_n, \tag{6}$$

where R_n is the reaction rate of reaction n. Note that the nucleation rate is a source term only for the negatively charged state of the first size section, for which the particle diameter equals ~ 0.5 nm.

The rate constants for coagulation between two nanoparticles are derived assuming that all nanoparticles lie in the free molecular regime, and strongly depend on the charge state of the nanoparticles. Two nanoparticles of the same charge will not coagulate because of their mutual Coulomb repulsion. The coagulation rates between charged and neutral nanoparticles are enhanced compared to neutral–neutral rates due to there being an induced image potential [31]. The coagulation rate between two nanoparticles 1 and 2 is

$$S_{coag,1,2} = f(z_1, z_2, r_1, r_2)\beta_{1,2}N_1N_2, \tag{7}$$

where z_i, r_i, and N_i are particle charge, radius, and number density of particle i, respectively. $\beta_{1,2}$ is the Brownian coagulation coefficient and $f(z_1, z_2, r_1, r_2)$ is a factor that

Table 2 Included in the model

Nucleation reaction	Rate constant ($cm^3\ s^{-1}$)[a]
$Si_2H_4B^- + SiH_4 \rightarrow NP + H_2$	4.83×10^{-11}
$Si_2H_4B^- + Si_2H_6 \rightarrow NP + H_2$	8.95×10^{-11}
$Si_2H_4B^- + SiH_2 \rightarrow NP + H_2$	4.95×10^{-11}
$Si_2H_5^- + Si_2H_4B \rightarrow NP + H_2$	9.02×10^{-11}
$Si_2H_5^- + SiH_4 \rightarrow NP + H_2$	4.83×10^{-11}
$Si_2H_5^- + Si_2H_6 \rightarrow NP + H_2$	8.92×10^{-11}
$Si_2H_5^- + SiH_2 \rightarrow NP + H_2$	4.93×10^{-11}
$Si_2H_5^- + Si_2H_4B \rightarrow NP + H_2$	8.99×10^{-11}
$Si_2H_5^- + SiH_3 \rightarrow NP + H_2$	4.88×10^{-11}
$Si_2H_5^- + Si_2H_3 \rightarrow NP + H_2$	9.02×10^{-11}
$Si_2H_5^- + Si_2H_5 \rightarrow NP + H_2$	8.95×10^{-11}

NP nanoparticle

[a] Rate coefficients are estimated to be 0.1 of the Langevin rate (see text)

accounts for nanoparticle charge. In the free molecular regime, the Brownian coagulation coefficient is given by

$$\beta_{1,2} = \left(\frac{3}{4\pi}\right)\sqrt{\frac{6k_BT}{\rho_p}\left(\frac{1}{v_1}+\frac{1}{v_2}\right)}\left(v_1^{1/3}+v_2^{1/3}\right)^2, \tag{8}$$

where ρ_p is the particle mass density, T is the temperature, and v_1, v_2 are the volumes of the two coagulating particles. The factor that accounts for particle charge effects on coagulation is given by

$$f(z_1,z_2,r_1,r_2) = \begin{cases} 1, & if\ z_1 = z_2 = 0 \\ 0, & if\ z_1 z_2 < 0 \\ E_{image}, & if\ z_1 \neq 0, z_2 = 0 \end{cases}, \tag{9}$$

where E_{image} represents the enhancement in coagulation due to the image potential induced in a neutral nanoparticle in proximity to a charged nanoparticle, as discussed in Ref. [39]. In a sectional model, each section represents a range of nanoparticle sizes. The coagulation rate between two sections cannot simply be calculated using the average diameter of each section, but has to be integrated over all sections as discussed in Ref. [35].

Surface growth occurs due to deposition of small radicals on the nanoparticle surface. We consider all monomer and dimer silicon hydride species as radicals in the surface growth model. The sticking coefficient on the nanoparticle surface is assumed to equal unity for all species except SiH (0.95), SiH_2 (0.8), SiH_3 (0.045), SiH_4 (10^{-5}), and Si_2H_6 (10^{-5}), as described in Refs. [40, 41]. Since two particles of the same charge do not collide at the temperatures of interest (<1000 K), negatively charged radicals can only deposit on neutral nanoparticles, while positive ions (SiH_3^+) can deposit on both neutral and negative nanoparticles. To simplify the reaction mechanism, we assumed that silicon nanoparticles represented by sections are bare silicon. In reality, a large fraction of the surface sites of nanoparticles may be occupied by hydrogen, which can affect sticking coefficients of radicals and nanoparticle growth. Molecular dynamics has been used to study the effects of hydrogen passivation of silicon nanoparticles (2–6 nm) on coagulation [42]. The source term due to surface growth is

$$S_{growth} = \frac{\dot{B}_j V_j}{\bar{v}_j} + \frac{\dot{C}_{j-1} V_j}{\bar{v}_j} - \frac{\dot{C}_j V_j}{\bar{v}_j}, \tag{10}$$

where $\dot{B}_j$ and $\dot{C}_j$ are the intra- and intersectional growth coefficients (in s^{-1}), V_j is total volume of particles in section j per unit volume of gas, and $\bar{v}_j$ is the average particle volume in section j. The rate of volume addition is expressed as

$$\dot{B}_j V_j = \dot{N}_s v_m \bar{A}_j N_{j,k}, \tag{11}$$

where $\dot{N}_s v_m$ is the linear growth rate (nm s^{-1}), v_m is the radical volume, and $\bar{A}_j$ is the average surface area in section j. The linear growth rate for species m with a particular nanoparticle size-charge is given by

$$\dot{N}_s = \alpha_{j,k,m} N_m \sqrt{\frac{8k_BT}{\pi m_m}} \tag{12}$$

where m_m is the radical mass and $\alpha_{k,m}$ is the collision frequency coefficient that accounts for radical-nanoparticle charge effects,

$$\alpha_{k,m} = \begin{cases} 1, & \text{if } z_k = z_m = 0 \\ 0, & \text{if } z_k z_m < 0 \\ 1 - \dfrac{z_k z_m e^2}{4\pi\varepsilon_0 \bar{R}_j k_B T}, & \text{if } z_k z_m > 0 \end{cases}, \tag{13}$$

where z_k is the nanoparticle charge, z_m is the radical charge, e the elementary charge, and $\bar{R}_j$ the average radius of section j. Intra- and inter-sectional growth coefficients are related by

$$\dot{C}_j = \dot{B}_j \frac{\bar{v}_{j+1}}{\bar{v}_{j+1} - \bar{v}_j}. \tag{14}$$

The distributions of charge within each size section are individually computed as different species. Only electron and ion attachment processes are taken into account in particle charging; that is, we do not consider secondary processes such as photo-electron emission or electric field emission. The charging probability density is defined as a one-step Markov process, where particle charge can only vary by ±1 charge at a time. The source term for particle charging for each size-charge combination is

$$S_{charging} = \sum_i I_i(k-1)N_{j,k-1} + I_e(k+1)N_{j,k+1} - \left[\sum_i I_i(k) + I_e(k)\right] N_{j,k}, \tag{15}$$

where I_i is the current to the nanoparticle of ion species and I_e is the electron current. Ion and electron currents to the particles are calculated from local plasma properties using Orbital Motion Limited theory [43], which is valid for small particles (<10 nm) in low-pressure plasmas. The thermal velocity distribution of ions is assumed to be Maxwellian. The collision frequency of electrons with nanoparticles is self-consistently calculated using rate coefficients provided by local solutions of Boltzmann's equation for the EED. Since the nanoparticles are included in the HPEM hierarchy in the same manner as other atoms and molecules in the plasma, their electron interactions are naturally included in the calculation of EEDs. Electron attachment and elastic cross sections with particles are from Ref. [20].

Nucleation and surface growth in this system occur via reactions among silicon hydrides. Bhandarkar et al. developed a zero-dimensional low-pressure model of silicon hydride plasma chemistry consisting of 300 species, Si_nH_m ($n < 10$), encompassing more than 6000 reactions [23]. Although that approach is insightful and may be more accurate from a kinetics perspective, including this large number of species and reactions in a 2-dimensional, plasma hydrodynamics model would be computationally prohibitive. In this model, we include 10 argon species, 3 helium species, 7 hydrogen species, and 18 silicon hydride species, Si_nH_m for $n \leq 2$, as listed in Table 1. The resulting hydrogen, argon, and helium chemistry is addressed with 165 reactions. Since the gas mixture is mostly composed of argon, the main source of electrons in the reactor comes from electron impact ionization of argon. Silicon hydride chemistry consists of 100 reactions. Reverse reaction rates are calculated based on Gibbs free energies that were found by ab initio calculations reported by Seal and Truhlar as shown in Table 3 (in a similar manner as described in Ref. [44]). Anion-neutral reaction rate constants are assumed to be lower than Langevin rate constants by one order of magnitude. Electron impact dissociation of silane mostly results from

Table 3 Change in Gibbs energy, ΔG (in kcal mol^{-1}) as computed at the G3SX(MP3)//M06-L/MG3S level of theory for each reagent at a partial pressure of 1 bar

Reaction	Temperature (K)							
	300	400	500	600	700	800	900	1000
SiH_4 (+M) → SiH_2 + H_2 (+M)	44.7	41.45	38.11	34.72	31.32	27.91	24.5	21.11
Si_2H_6 (+M) → SiH_4 + SiH_2 (+M)	43.36	40.1	36.89	33.73	30.62	27.55	24.53	21.55
Si_2H_6 (+M) → H_2 + Si_2H_4B (+M)	42.72	39.09	35.39	31.66	27.91	24.16	20.42	16.69
Si_2H_4B (+M) → Si + SiH_4 (+M)	37.11	35.45	33.83	32.24	30.69	29.16	27.65	26.16
Si + Si_2H_6 → SiH_2 + Si_2H_4B	6.25	4.65	3.06	1.48	−0.07	−1.61	−3.12	−4.61
SiH_2 (+M) → Si + H_2	36.47	34.44	32.34	30.18	27.98	25.77	23.53	21.29
H + SiH_4 → H_2 + SiH_3	−15.38	−16.07	−16.77	−17.46	−18.15	−18.82	−19.47	−20.1
SiH_2 + SiH_2 → Si_2H_2 + H_2	−19.15	−18.6	−18.15	−17.76	−17.43	−17.13	−16.86	−16.6
H + Si_2H_6 → SiH_4 + SiH_3	−16.73	−17.42	−17.99	−18.46	−18.85	−19.17	−19.44	−19.65
H + Si_2H_6 → Si_2H_5 + H_2	−18.58	−19.39	−20.2	−21	−21.79	−22.56	−23.31	−24.03
SiH_3 + SiH_3 → SiH_2 + SiH_4	−23.01	−22.48	−21.93	−21.37	−20.8	−20.23	−19.66	−19.09
SiH_4 + SiH_3 → Si_2H_5 + H_2	−1.85	−1.96	−2.2	−2.54	−2.94	−3.39	−3.87	−4.38
SiH_4 + SiH → Si_2H_3 + H_2	−2.02	−2.47	−3.05	−3.7	−4.4	−5.15	−5.92	−6.71
SiH_2 + H → SiH + H_2	−28.44	−28.47	−28.5	−28.53	−28.555	−28.562	−28.557	−28.53
SiH_3 (+M) → SiH + H_2 (+M)	31.64	29.05	26.37	23.66	20.91	18.17	15.41	12.67
SiH + SiH_4 → Si_2H_4B + H	27.81	27.47	27.01	26.46	25.84	25.17	24.44	23.67
SiH_3 + H → SiH_2 + H_2	−38.39	−38.54	−38.69	−38.83	−38.95	−39.05	−39.13	−39.19
Si_2H_2 → Si_2 + H_2	35.16	32.92	30.66	28.38	26.11	23.85	21.59	19.36
Si_2H_4B → Si_2H_2 + H_2	32.26	29.37	26.42	23.45	20.47	17.5	14.54	11.6
SiH_3 + SiH_3 → Si_2H_6	−66.36	−62.57	−58.81	−55.09	−51.42	−47.79	−44.2	−40.64
SiH_2^- + SiH_4 → $Si_2H_4B^-$ + H_2	−12.78	−12.8	−12.92	−13.13	−13.41	−13.72	−14.07	−14.45
SiH_2^- + SiH → SiH_2 + SiH^-	9.29	9.57	9.86	10.15	10.44	10.74	11.03	11.33
SiH_2^- + SiH_3 → SiH_2 + SiH_3^-	−8.81	−8.53	−8.25	−7.97	−7.69	−7.41	−7.13	−6.85
SiH_2^- + Si_2H_3 → SiH_2 + $Si_2H_3^-$	−30.74	−30.22	−29.69	−29.15	−28.6	−28.05	−27.5	−26.94

Table 3 continued

Reaction	Temperature (K)							
	300	400	500	600	700	800	900	1000
$SiH_2^- + Si_2H_5 \rightarrow SiH_2 + Si_2H_5^-$	−19.3	−18.96	−18.62	−18.27	−17.92	−17.58	−17.24	−16.89
$Si_2H_4B^- + SiH \rightarrow Si_2H_4B + SiH^-$	21.43	21.36	21.29	21.21	21.14	21.06	20.99	20.92
$Si_2H_4B^- + SiH_3 \rightarrow Si_2H_4B + SiH_3^-$	3.34	3.26	3.18	3.09	3.01	2.92	2.83	2.73
$Si_2H_4B^- + Si_2H_3 \rightarrow Si_2H_4B + Si_2H_3^-$	−18.59	−18.43	−18.26	−18.09	−17.91	−17.73	−17.54	−17.36
$Si_2H_4B^- + Si_2H_5 \rightarrow Si_2H_4B + Si_2H_5^-$	−7.15	−7.17	−7.19	−7.21	−7.23	−7.25	−7.28	−7.31
$SiH_3^- + SiH_4 \rightarrow Si_2H_5^- + H_2$	−12.34	−12.39	−12.57	−12.84	−13.18	−13.56	−13.98	−14.42
$SiH_3^- + SiH_2 \rightarrow Si_2H_3^- + H_2$	−37.01	−36.57	−36.22	−35.95	−35.73	−35.54	−35.38	−35.23
$SiH_3^- + SiH_3 \rightarrow Si_2H_4^- + H_2$	−26.99	−26.74	−26.6	−26.53	−26.52	−26.55	−26.61	−26.69

The unimolecular reagents are assumed to be fully equilibrated (i.e., to be in the high-pressure limit)

$$\begin{cases} e + \mathrm{SiH_4} \rightarrow \mathrm{SiH_2} + 2\mathrm{H} + e \\ e + \mathrm{SiH_4} \rightarrow \mathrm{SiH_3} + \mathrm{H} + e \end{cases} \quad (16)$$

where cross sections were obtained from Ref. [40].

We assume that all nanoparticles are spherical, implying that coagulating nanoparticles immediately coalesce, preventing the formation of nonspherical agglomerates. Since we are not addressing the morphology of the particles, an agglomerated particle and a coagulated particle are treated the same in the model. This is probably reasonable considering the small size of the nanoparticles treated.

Computational Challenges

The model developed in this study is computationally intensive. The model solves for plasma and neutral transport, temperatures and Poisson's equation using a combination of explicit, semi-implicit and implicit methods with time steps calculated based on instantaneous plasma properties or a fraction of the RF period. A typical time step used to maintain numerical stability and resolve the RF period is 10^{-10} s. Noting that the residence time for gas flow through the tube is 5–10 ms, we would expect to reach full convergence after over 10 ms of integration.

Since here we are most interested in quasi-steady state properties, the rate of convergence is improved by better estimates for the initial conditions of species. Estimating initial conditions for the spatial distribution of the section densities is made difficult by the complexity of the reaction mechanism. Since it takes significant time for nanoparticles to grow to higher sections by surface growth and coagulation, we introduced a *boost* option which establishes better initial conditions than other estimation methods. When boosting is enabled, nucleation and surface growth rate coefficients are artificially increased by a factor F_b for a time T_b, after which the option is disabled and rate coefficients are returned to their normal values. There is no physical rationale to the boosting other than to provide better initial conditions for the time integration at reduced computational cost. For the conditions of this study, we used $F_b = 50$ and $T_b = 20\,\mu\mathrm{s}$. A transient does occur in the densities of all species when terminating boosting. After an extensive sensitivity study, the values F_b and T_b were chosen to minimize the transient and minimize any systematic effects on the final distributions of nanoparticles.

A significant amount of computational time is consumed by the exchange terms for momentum and energy in Eqs. (3) and (4). These exchange terms for each species are sums over all other species at every mesh point, and so scale as n^2, where n is the number of species. In practice, the exchange terms between species that have small mole fractions make negligible contributions to the total rate of momentum or energy exchange because their mutual collision frequencies are so small. From a practical matter, in a fluid simulation momentum transfer collision terms are only important between species for which at least one of the collision partners has a reasonably large mole fraction. To reduce the computational burden, we computed momentum and temperature exchange terms only for pairs of species for which at least one of the partners has a mole fraction larger than a specified value. After a sensitivity study, we found that an optimum value with respect to speed-up and accuracy is a mole fraction of 10^{-3}.

In order to benefit from multicore computer architectures, algorithms in the HPEM were parallelized using OpenMP directives [45]. Since the HPEM consists of many different modules each having separate algorithms which are executed sequentially for relatively

short times, it is difficult to amortize the computational overhead in launching parallel threads. For this particular implementation of the HPEM, the overall speedup gained with respect to serial execution is shown in Fig. 1a, and is 2.6 on 12 cores using the Intel Fortran Compiler and 2.8 GHz Intel Xeon processors.

The single most compute-intensive calculation in the HPEM is solution of an elliptic equation for electrostatic potentials—Poisson's equation. In the HPEM this solution is cast in semi-implicit form where the charge density at future times is estimated based on current values of densities, fluxes and transport coefficients [34]. The method of successive over relaxation (SOR) can be an efficient method for obtaining a rapid and sufficiently accurate solution. To improve the computational speed of the SOR solver in the HPEM, we implemented a multigrid algorithm which reduces the number of iterative steps needed for solution of Poisson's equation. This technique was implemented for both the 5-point

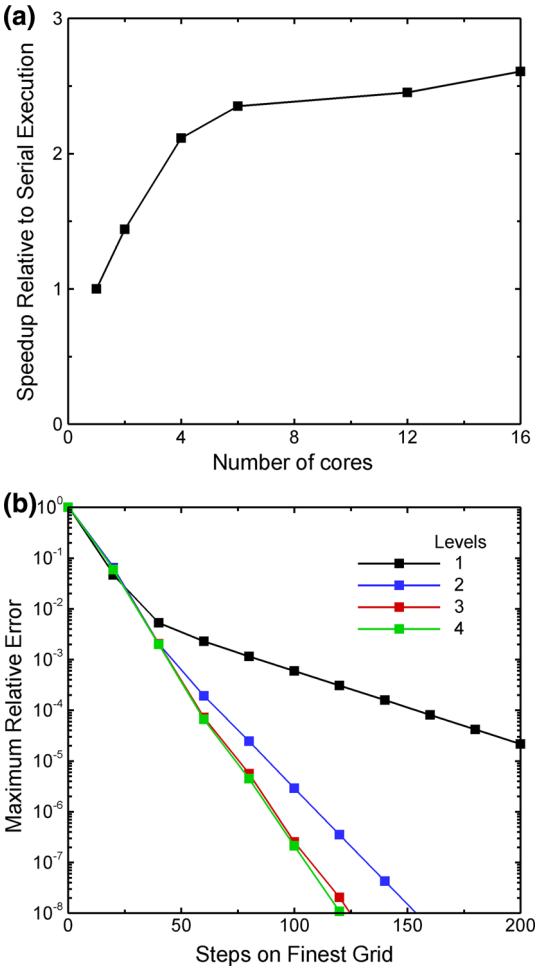

Fig. 1 Computational metrics. **a** Overall speedup of the model relative to serial execution. **b** Reduction of the maximum fractional error with iteration number for the original Red–Black solver on a uniform mesh (nLevels = 1) and for the new multigrid version of the same Red–Black scheme using from 2 to 4 levels

stencil used for non-magnetic electrostatic solutions and for the 9-point stencil used when magnetic cross terms are implemented. (The mesh is structured and rectilinear.) In both cases, a Red–Black form of the Gauss–Seidel scheme is used, which both conditions the equations and facilitates a thread-parallel iterative solver.

The reduction in the maximum fractional error is shown in Fig. 1b as a function of iteration number for the original Red–Black solver on a uniform mesh (nLevels = 1) and for the new multigrid version of the same Red–Black scheme using from 2 through 5 levels [46]. The rate of convergence significantly increases with even 2 levels, and continues to improve up to about 4 levels. For this problem the number of full mesh iterations needed to reduce the error by a factor of 10^8 is reduced from 720 iterations (original SOR method) down to about 120 iterations (multigrid with 4 levels).

The new multigrid method for HPEM was structured for computational efficiency and scalability on multi-core processors. Coefficient and field arrays are copied into work arrays which are structured to organize computation into long vector loops with many concurrent arithmetic operations to fully take advantage of vector architectures. Good thread-parallel efficiency is achieved by pinning threads to cores and using first touch to commit memory assigned to work arrays to be local to the cores within the processor [47]. The multigrid approach reduced SOR times by a factor of 5 in both serial and parallel operation.

In the next section, we report simulation results after 6 ms. A fully converged solution (achieved after tens of milliseconds) might slightly differ quantitatively from the results presented here. However, we expect simulations to be advanced enough in time that we do not expect any qualitative differences.

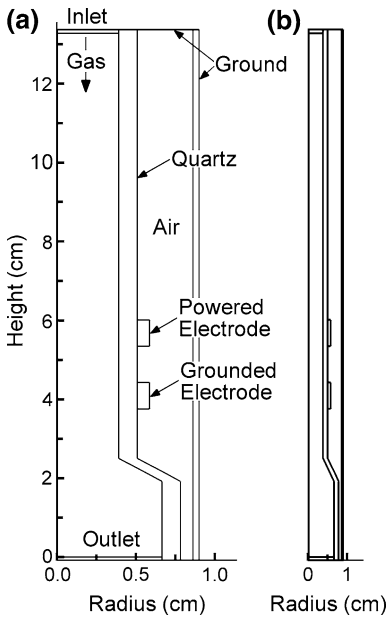

Fig. 2 Schematics of the geometry used in our model. **a** Radius expanded by a factor of 4. **b** Actual geometry

Particle Synthesis in RF Discharges: Base Case

The geometry used in the model is shown in Fig. 2a and is patterned after the experiments reported in Ref. [11]. Due to the high aspect ratio of the reactor, the radial dimension in all two-dimensional figures is scaled by a factor of four, shown in Fig. 2b, to enable details to

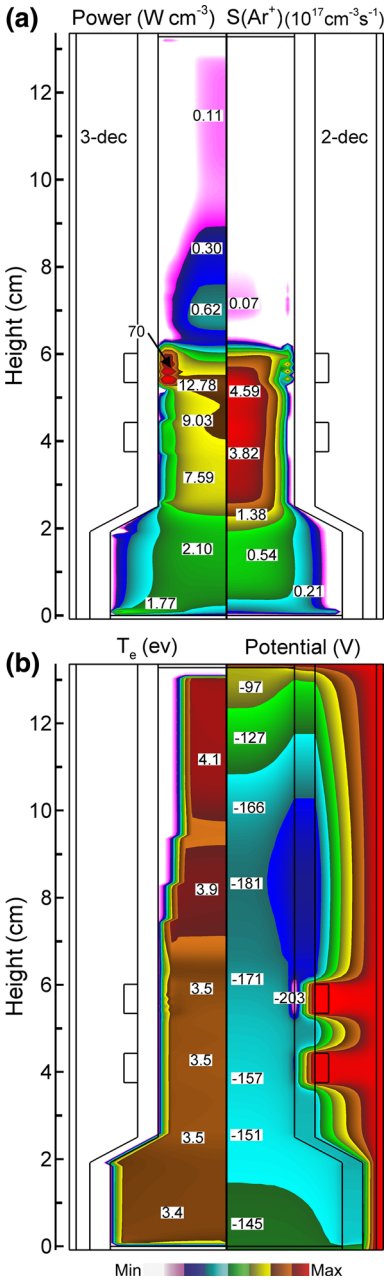

Fig. 3 Plasma properties for the base case conditions (Ar/He/SiH_4 = 50/4.75/0.25, 1.5 Torr, 3 W, 50 sccm). **a** Power deposition and Ar^+ source by electron impact, **b** electron temperature and electric potential. Log-scale plots have number of decades noted

be resolved. The plasma reactor consists of a narrow quartz tube that starts at 0.8 cm inner diameter and 1 cm outer diameter (wall thickness of 0.1 cm). Gas is injected from the top and pumped out from the bottom. The tube expands to 1.4 cm inner and 1.6 cm outer diameter 2 cm below the electrodes. The upper electrode is powered at an RF frequency of 25 MHz and deposits a specified 1–5 W in the plasma. The voltage amplitude applied to the powered electrode is adjusted to deliver the desired power. The inlet gas is a mixture of argon, helium and silane. Experiments have shown that varying the flow rate, which varies the residence time in the reactor, produces different nanoparticle sizes [48]. In this investigation, the typical argon flow rate was 25–100 sccm. Nanoparticle deposition on the walls of the reactor is observed in experiments [11], and so neutral nanoparticle sticking coefficients with the wall are set to unity.

This particular geometry represented challenges in solving Poisson's equation consistent with the experimental apparatus and the observation that particles flow out of the reactor. The actual reactor has a large diffusion zone at the bottom of the geometry shown in Fig. 2. The actual size of the experimental diffusion zone could not be addressed by the model. Solution of Poisson's equation requires boundary conditions on the edge of the numerical mesh. This boundary condition is typically of the Dirichlet type, specifying the electric potential on the boundary. Doing so artificially trapped negatively charged particles in the computational domain near the pump port where gas flow pushed particles into the electrostatic repulsion produced by the sheaths formed at the boundary. To address this issue, a Neumann boundary condition was implemented at the pump port for Poisson's equation and charged particle fluxes to enable their flow out of the system.

Under plasma conditions corresponding to these simulations, experiments produce up to 2–3 nm-diameter particles [48]. The sectional model uses 55 sections with a spacing factor, defined in Eq. (1), of $a = 1.15$ [30]. The lower nanoparticle diameter of the first section equals 0.49 nm, which corresponds to 3 Si atoms assuming the mass density of bulk silicon. Due to the particle charge limit, only one electron can be attached to a Si particle of size up to 2.4 nm diameter [28]. The total number of charge-size species within the sectional model therefore equals 90. The base case conditions were based on typical experiments [48]. The input gas mixture was Ar/He/SiH_4 = 50/4.75/0.25 sccm at the inlet. (The silane used in the experiments that motivated this work was diluted in helium. The inclusion of He in the model was merely to follow experimental conditions. Since the threshold energies for exciting and ionizing the helium are larger than those for the Ar and SiH_4, very little power is expended in producing excited states and ions of helium. The densities of excited states and ions of helium are, in fact, negligible in the model.) The pressure was kept constant at 1.5 Torr by adjusting the flow rate out of the reactor. The wall temperatures were held constant at 325 K and the power deposited in the plasma was 3 W.

Spatial profiles of power deposition and the electron impact ionization source for Ar^+ are shown in Fig. 3. At the frequencies and pressures of interest, power deposition is largely into electrons by the oscillating electric field of the sheath. Most of the power is deposited within 1 mm of the boundary in the vicinity of the powered (top) electrode, with a maximum value of 70 W cm^{-3}. Two minor peaks in power deposition, about 10 W cm^{-3} between 4 and 6 cm, are caused by Joule heating in the bulk plasma, and result from the positioning of the electrodes and division of the conduction and displacement currents. Electron impact ionization of argon is the dominant ionization source in the plasma due to the large overall mole fraction of argon. The double peaks in the ionization rate correspond to that of the power deposition.

The densities of electrons, negative ions, total positive ions and total negative nanoparticles are shown in Fig. 4. The electron density peaks at 2.0×10^{12} cm^{-3} along the centerline between the two electrodes. Total positive and negative ion densities peak at 1.9×10^{12} and 1.8×10^{12} cm^{-3}, respectively. The spatial extent of the electron density is

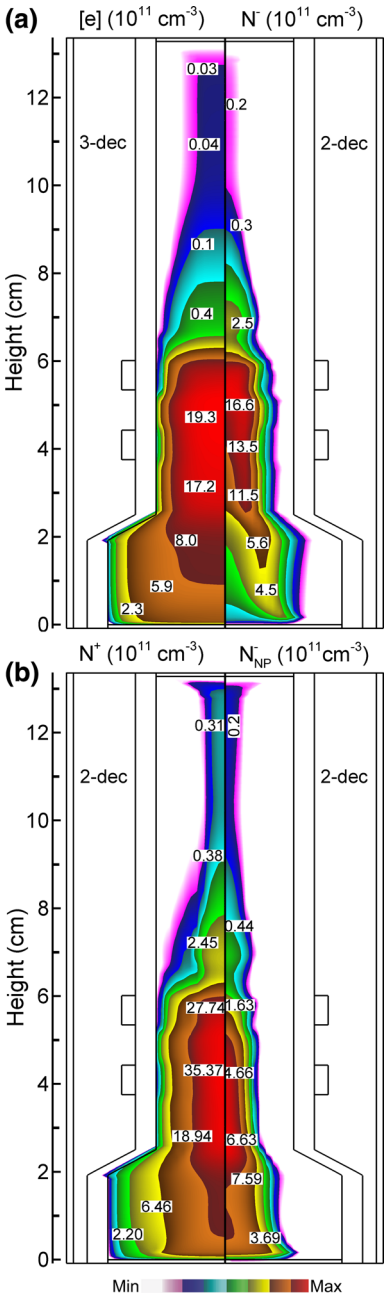

Fig. 4 Charged particle densities for the base case conditions (Ar/He/SiH_4 = 50/4.75/0.25, 1.5 Torr, 3 W, 50 sccm). **a** Electron and total negative ions, **b** total positive ions and total negative nanoparticles. Plots are log-scale with number of decades noted

largely confined to between the electrodes where the power deposition is large. Downstream of the electrodes, the balance between positive ions and negative charge is largely maintained by negative ions and negatively charged nanoparticles. Note that the lighter, negative ions extend to a larger radius than the heavier nanoparticles. Due to the lower mobility and diffusivity of the nanoparticles, they tend to respond to the time-averaged

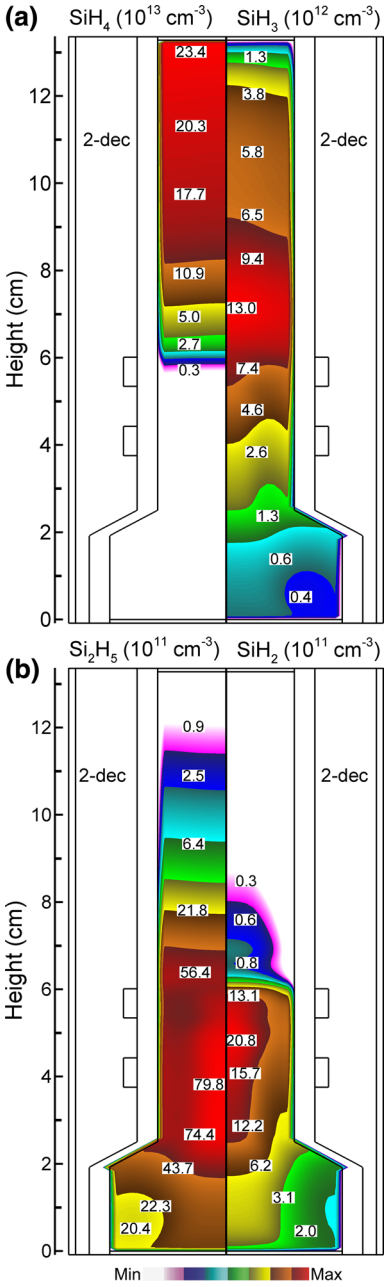

Fig. 5 Silicon hydride densities for the base case conditions ($Ar/He/SiH_4 = 50/4.75/0.25$, 1.5 Torr, 3 W, 50 sccm). **a** SiH_4 and SiH_3, **b** Si_2H_5 and SiH_2. Plots are log-scale with number of decades noted

potentials, which, in this case, have a maximum on axis. Electron depletion is not significant here due to the small size of the nanoparticles that typically hold only one negative charge or are neutral. In dusty plasmas that contain larger particles, the electron density can be significantly depleted by charging of the nanoparticles [30]. The dense plasma region extends to 2 cm below the electrodes as observed experimentally [11]. However, experimental electrostatic capacitive probe measurements report ion densities in the range 10^{10}–10^{11} cm^{-3}, which is less that we find from our model. This discrepancy may be due to uncertainties in actual power deposition into the plasma due to matching issues from the power supply. The electron temperature is near 3.5 eV throughout the plasma region, as shown in Fig. 3b. This somewhat high electron temperature results from the consumption of electrons due to charging of nanoparticles, which then requires more ionization (produced by a higher electron temperature) to compensate [49].

With the voltage being applied to one electrode, the second electrode being grounded and the discharge surrounded by electrical ground, the discharge is asymmetric and a dc bias forms to balance the RF currents. In the model, there is a 20 nF blocking capacitor in series between the power supply and the discharge tube. Between the blocking capacitor and the plasma, there is the additional series capacitance of the electrode-tube-plasma sandwich, which is about 5 pF. Since the blocking capacitor is much larger than the capacitance of the electrode, the dc bias appears dominantly across the discharge tube under the powered electrode (see Fig. 3b). Since the blocking capacitance in most impedance matching networks is typically much larger than 5 pF, we expect the same distribution of dc bias voltage in the experiments.

Since overall the plasma is electropositive on an RF-period average, we expect negatively charged particles to be radially confined along the centerline. However, the electric potential monotonically increases in the axial direction from the electrode region to the outlet which, experimentally, is afforded by the large diffusion chamber downstream (and is approximated by our boundary conditions at the pump port). This overall gradient in potential works against trapping of negative nanoparticles in the axial direction and enables them to flow out of the reactor. The lifetime of negative nanoparticles is still lengthened compared to those of neutral nanoparticles due to their electrostatic trapping in the radial direction, preventing their deposition on the tube walls. However, since nanoparticles are

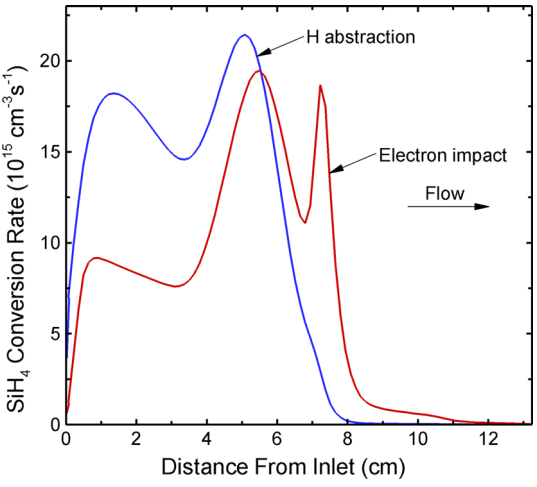

Fig. 6 Rate of SiH_4 conversion to products by electron impact and hydrogen abstraction reactions

not necessarily trapped in the axial direction, their residence time on average is close to the background gas residence time. This observation agrees with experiments, in which the sizes of nanoparticles are tuned by varying the background gas flow rate which translates into residence time [48].

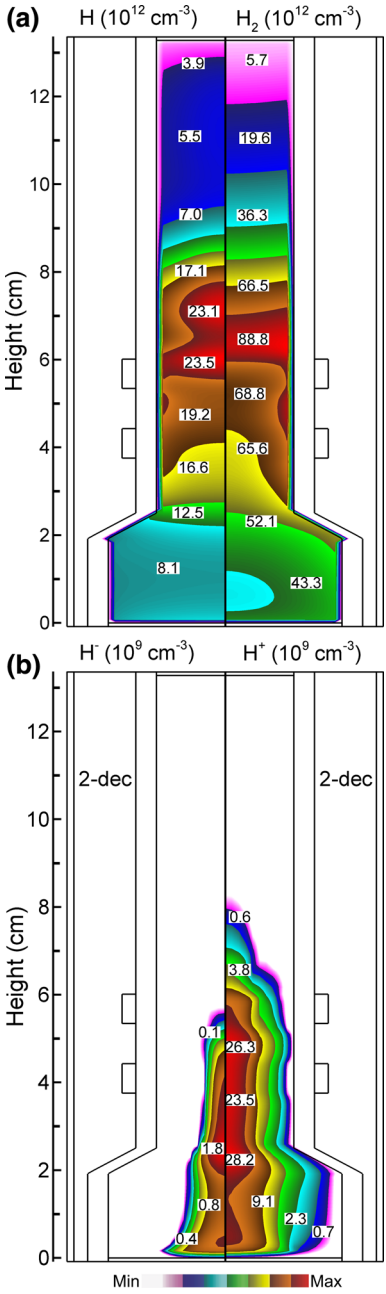

Fig. 7 Atomic and molecular hydrogen densities for the base case conditions ($Ar/He/SiH_4$ = 50/4.75/0.25, 1.5 Torr, 3 W, 50 sccm). **a** H and H_2, **b** H^- and H^+. Log-scale plots have number of decades noted

The densities of silicon hydride species that are important for nanoparticle formation and growth are shown in Fig. 5. The density of SiH_4 is 2.2×10^{14} cm^{-3} at the inlet before its density is reduced by electron impact dissociation and hydrogen abstraction reactions while flowing through the tube. The rates of silane conversion to products and hence radical production, along the centerline due to electron impact and hydrogen abstraction are shown in Fig. 6. Hydrogen abstraction reactions are more important than electron impact dissociation in the upstream part of the tube, where the H density is three orders of magnitude greater than the electron density. Between the two electrodes, the SiH_4 density is four orders of magnitude smaller than at the inlet. The majority of this decrease is by dissociation though some is also due to rarefaction by gas heating. The densities of SiH_2, SiH_3, and Si_2H_5 peak at 1.9×10^{12}, 1.2×10^{13}, and 6.4×10^{12} cm^{-3} respectively, increasing in density downstream as the SiH_4 is dissociated while flowing from the inlet. The advective speed of gas flowing through the tube is 1.8 m s^{-1} along the centerline, and so there is some back diffusion of species towards the inlet.

Electron impact dissociation of SiH_4 produces both SiH_2 (silylene) and SiH_3 (silyl) in reactions that also produce atomic H. The H atoms can then abstract H from SiH_4 to produce another SiH_3. At low pressure, the rate of reaction of SiH_3 with other species is fairly low, and so silyl will persist in the discharge. SiH_2 will rapidly insert into SiH_4 to produce disilane, Si_2H_6, and so silylene is quickly consumed in regions where the SiH_4 density is high. The rate of consumption is $>10^{15}$ cm^{-3} s^{-1} in the vicinity of the powered electrode. SiH_2 will also rapidly insert into other saturated silanes, Si_nH_{2n+2}, to produce the next higher silane, $Si_{(n+1)}H_{2(n+1)+2}$. H atom abstraction from Si_2H_6 produces Si_2H_5 ($>10^{15}$ cm^{-3} s^{-1} in the electrode region). These differences in reactivity in large part explain the different spatial distributions of SiH_2 (small where the density of SiH_4 is still large), SiH_3 (extending to the inlet nozzle where SiH_4 is initially dissociated), and Si_2H_5 (large around the electrodes where SiH_4 is low).

The densities of hydrogen species H, H_2, H^- and H^+ are shown in Fig. 7. The densities of H and H_2 have maximum values of 2.3×10^{13} and 8.8×10^{13} cm^{-3}, respectively. H is predominantly produced through electron impact dissociation of SiH_4 while H_2 is largely produced by hydrogen abstraction from SiH_4. Both sources rely on SiH_4 and so the associated production rates are largest upstream of the electrodes prior to SiH_4 being fully dissociated. The H_2 density is larger than that of H due to the propensity of H atoms to participate in the H abstraction reactions (which decreases the H density) that produce H_2. The experimental H density was estimated from measurements of optical emission from the plasma and is $\approx 10^{13}$ cm^{-3} [11]. H^- and H^+ densities peak along the centerline at the expansion of the tube, with values of 2.2×10^9 and 2.8×10^{10} cm^{-3}, respectively. Both of these ions are produced by electron impact. H^+ is predominantly produced by ionization of H, while H^- comes from dissociative attachment of H_2^+ ($e + H_2^+ \rightarrow H^- + H^+$) [50]. Since atomic H is abundant in this system, the density of H^+ is greater than that of H^-. The H^- density peaks in the expansion zone, while H^+ is more spread between the electrodes due to the ambipolar electric field which accelerates positive ions towards the walls while confining the negative ions.

All of these radicals play a role in the surface growth of nanoparticles. However, based on the hierarchy of sticking coefficients, we expect SiH_2 and Si_2H_5 to be the dominant radicals contributing to surface growth, with SiH_3 playing a less important role. The density of $Si_2H_4^-$ peaks at 3.3×10^{10} cm^{-3} below the bottom electrode, while the $Si_2H_5^-$ density peaks at 8.0×10^{11} cm^{-3} between the two electrodes. Therefore, nucleation mostly occurs through the $Si_2H_5^-$ pathway. SiH_3^+, the only positively charged silicon

hydride species we consider in the reaction mechanism, has a maximum density of 7.3×10^{10} cm^{-3} between the two electrodes.

The nucleation rate, surface growth rate, coagulation rate, and total nanoparticle density are shown in Fig. 8. The nucleation rate (defined as the rate of formation of silicon hydride

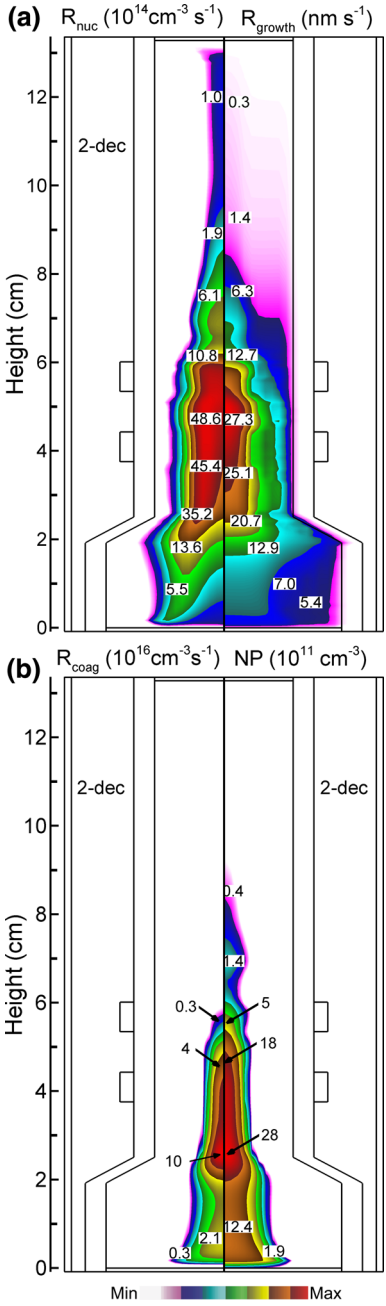

Fig. 8 Nanoparticle growth mechanisms. **a** Nucleation rate and surface growth rate, **b** coagulation rate and total nanoparticle density. Log-scale plots have number of decades noted

anions containing at least 3 Si atoms) peaks at 4.5×10^{15} cm^{-3} s^{-1} between the two electrodes. $Si_2H_5^-$ is the dominant species for nucleation as its density is significantly higher than that of $Si_2H_4^-$. Nucleation in this mechanism is dominated by negative ion–molecule reactions, and the net axial electric field produces a drift of negative ions downward. Therefore, the local nucleation at the top of the tube must result from negative ions formed locally. The dominant reactions leading to particle nucleation are shown in Fig. 9a. $Si_2H_5^-$ reacts with SiH_4 in the upstream portion of the tube prior to SiH_4 being dissociated. As the density of Si_2H_6 increases, largely due to the consumption of SiH_4 through SiH_2 insertion, the reaction with Si_2H_6 then dominates. The nucleation and surface growth rates are both maximum near the center of the electrodes. This represents an important difference between nonthermal plasmas and neutral aerosols, as discussed in [51]. In neutral aerosol systems surface growth tends to quench nucleation, because nucleation and surface growth compete for the same radical species. However in

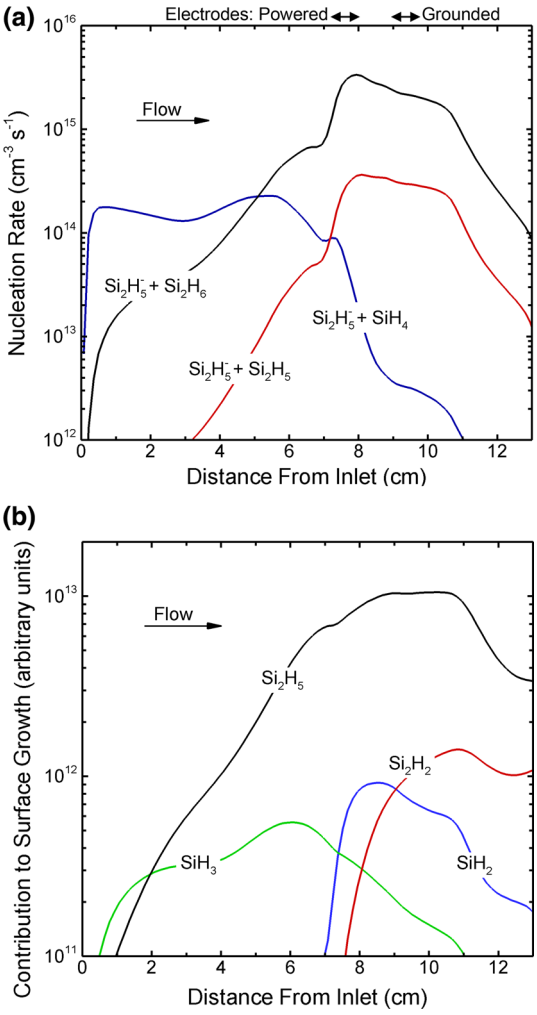

Fig. 9 Contributions to particle growth. **a** Nucleation reaction rates for reactions involving $Si_2H_5^-$ species and **b** relative contribution of radical deposition on nanoparticle surfaces during surface growth

nonthermal plasmas, where most particles are negatively charged, anions, which are important for nucleation, are relatively unimportant for surface growth, except for the typically much smaller populations of neutral and positive nanoparticles. Hence surface growth does not quench nucleation, and the nucleation and surface growth rates are both closely coupled to electron impact collisions—either forming ions or radicals through dissociation. Since the electron density is maximum near the center of the electrodes, the nucleation and surface growth rates also peak near the same location.

The overall surface growth rate average over all size-charge nanoparticles peaks at 29.3 nm s^{-1} between the electrodes where the densities of radicals are maximum. The relative contributions of radical species to surface growth are shown in Fig. 9b. The dominant species contributing to surface growth is Si_2H_5 even though the densities of SiH_3 and SiH_2 are comparable to that of Si_2H_5. The sticking coefficient of SiH_3 on nanoparticle surfaces is estimated to be 0.045, compared to a value of unity assumed for Si_2H_5. But even for equal sticking probabilities, Si_2H_5 contributes two Si atoms to particle growth and so will have a proportionately larger contribution compared to SiH_x. The rate of surface

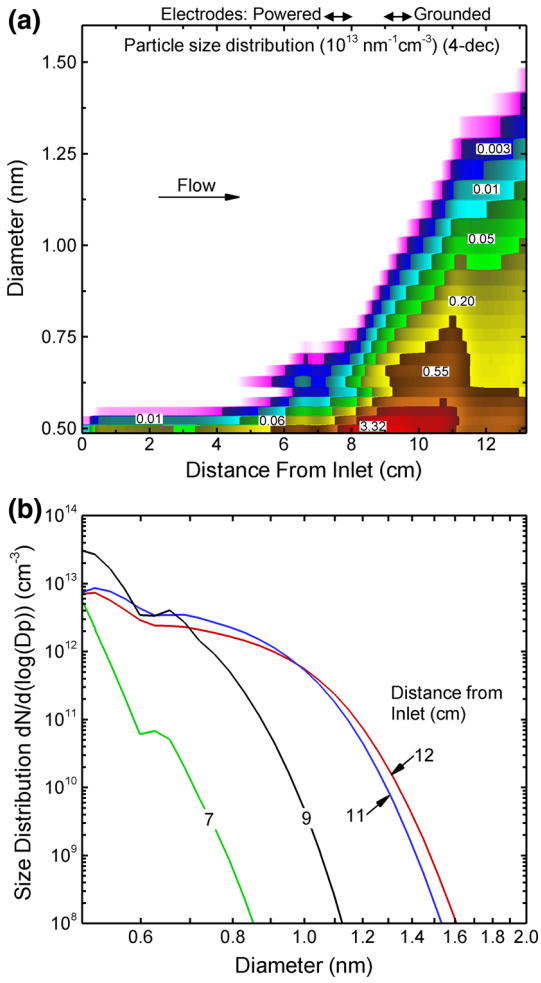

Fig. 10 Nanoparticle size distributions on the centerline of the reactor (r = 0). **a** Nanoparticle size distribution (cm^{-3} nm^{-1}) over 4 decades as a function of distance from the inlet, and **b** size distribution at 7, 9, 11 and 12 cm from the inlet

growth remains relatively high below and downstream of the bottom electrode in large part due to the convection downstream of radicals produced in the more intense plasma between the electrodes. Based only on the surface growth rate, particles of a few nm would require many tens of ms to form, which considerably exceeds the gas residence time. Therefore, coagulation must play an important role in particle growth.

The total nanoparticle density is the sum of all nanoparticles regardless of size or charge and has a maximum value of 2.3×10^{12} cm^{-3} where the tube starts to expand. The total density is dominated by the larger density of the smallest particles. The particle size distribution along the centerline of the tube is shown in Fig. 10a. Nucleation predominantly occurs between the electrodes and particles grow while flowing towards the outlet. The evolution of the particle size distribution along the centerline as a function of distance from the inlet is shown in Fig. 10b. The density of the smallest nanoparticles increases from 7 to 9 cm from the inlet as particles nucleate and flow through the tube. Their densities decrease from 9 to 11 cm from the inlet because of the expansion of the tube which leads to a spreading of the nanoparticle cloud by radial diffusion (see Fig. 8b). From 11 to 12 cm from the inlet, the size distribution shifts to larger sizes as the nucleation rate drops (Fig. 8a) and particles grow.

Particle size distributions for negatively charged and neutral nanoparticles at the outlet on the centerline are shown in Fig. 11. The total density of negative nanoparticles is approximately one order of magnitude larger than for neutral nanoparticles over the range of particle sizes. The total coagulation rate is the sum of rates of coagulation between all possible combinations of particle charge and size, and is shown in Fig. 8b. This rate peaks at 1.2×10^{17} cm^{-3} s^{-1} on the centerline at the beginning of the expansion zone where the negative and neutral nanoparticle densities are the highest. By far the largest contribution to the coagulation rate is due to coagulation between negative and neutral nanoparticles. Each such coagulation event consumes one neutral nanoparticle, while creating a larger negative nanoparticle. The typical particle sizes observed in similar experiments are 1–3 nm [11], and so our predictions here somewhat underestimate those particle sizes. The major uncertainty in setting values for the model is estimating the actual power deposition in the plasma that occurs in the experiment (the reflected power is not measured). The major uncertainties in the model are the sticking coefficients of radical species on the

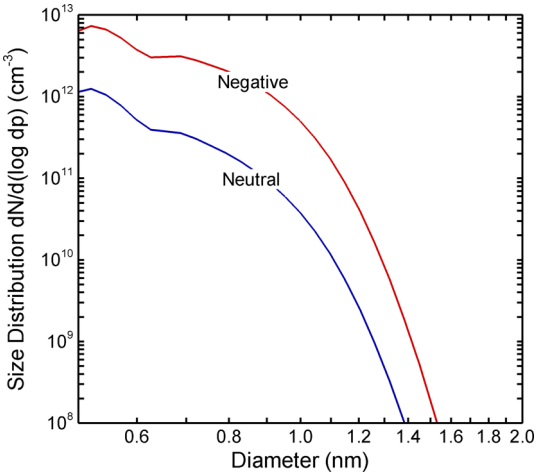

Fig. 11 Size distributions for negatively charged and neutral nanoparticles at 11 cm from the inlet on the centerline

growing nanoparticles. The best available values for those coefficients were used in this investigation, and so there is likely room for improvement in those values.

Nanoparticle Temperature and Crystallization

The experiments which form the basis of this modeling study produce both amorphous and crystalline silicon nanoparticles [11, 48]. The temperatures at which nanoparticles crystallize are a sensitive function of size—for example, 773 K for 4-nm and 1273 K for 10-nm-diameter silicon particles [15]. These crystallization temperatures are higher than the gas temperatures both observed in experiments and predicted in this study. Experimental and numerical studies have shown that exothermic surface processes (e.g., ion recombination and hydrogen reactions) on the surface of the nanoparticle are likely responsible for crystallization by heating the particle above its crystallization temperature [16, 48, 52]. For purposes of discussion, nanoparticle temperature is intended to represent the particle's internal or bulk temperature, and is distinct from the particle's translational temperature.

To investigate the spatial dependence of the internal temperature of nanoparticles, a Monte Carlo model similar to that developed by Mangolini and Kortshagen [16] was implemented. The rate of change of the nanoparticle temperature was computed by

$$\frac{4}{3}\pi R^3 \rho_p C_p \frac{dT_p}{dt} = G - L, \tag{17}$$

where ρ_p is the silicon mass density, C_p is the heat capacity, G is the rate of heating, and L the rate of cooling by thermal conduction to the gas. One of the heating processes is

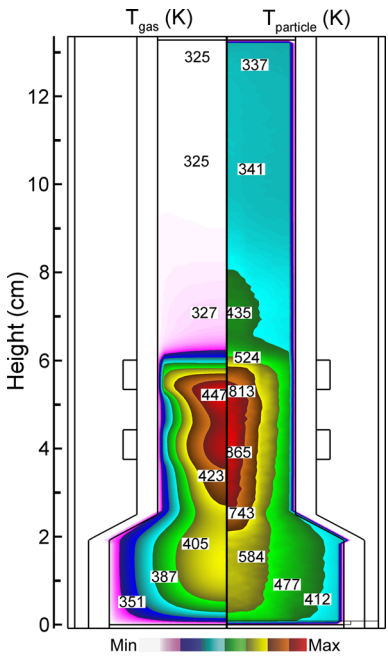

Fig. 12 Temperatures for the base case conditions: (*left*) gas temperature (325–445 K) and (*right*) internal temperature (325–866 K) for 2 nm-diameter nanoparticles

recombination of argon ions on the surface of the particle, which delivers 15.6 eV of energy to the particle (the ionization potential of Ar). Hydrogen surface reactions include H atom passivation of dangling bonds, depositing 3.1 eV (the energy of the Si–H bond) into the particle; H-induced abstraction through the Eley–Rideal mechanism, depositing 1.41 eV; and physical adsorption of H, depositing either 3.1 eV (recombination with a dangling bond) or 4.51 eV (recombination with an incoming radical) [16]. The internal energy of the particle is mostly dissipated by thermal conduction with the background gas, which is mainly argon in this work. Statistical averages for particle temperatures at each numerical mesh point were obtained by following trajectories of over 10^5 collisions of ions and H atoms with a nanoparticle. For purposes of computing internal temperatures, nanoparticle transport was neglected as the conduction time scale is small compared to the time scale for transport.

Using the Monte Carlo model, local plasma properties provided by the plasma hydrodynamics model were used to predict the nanoparticle internal temperatures. The gas

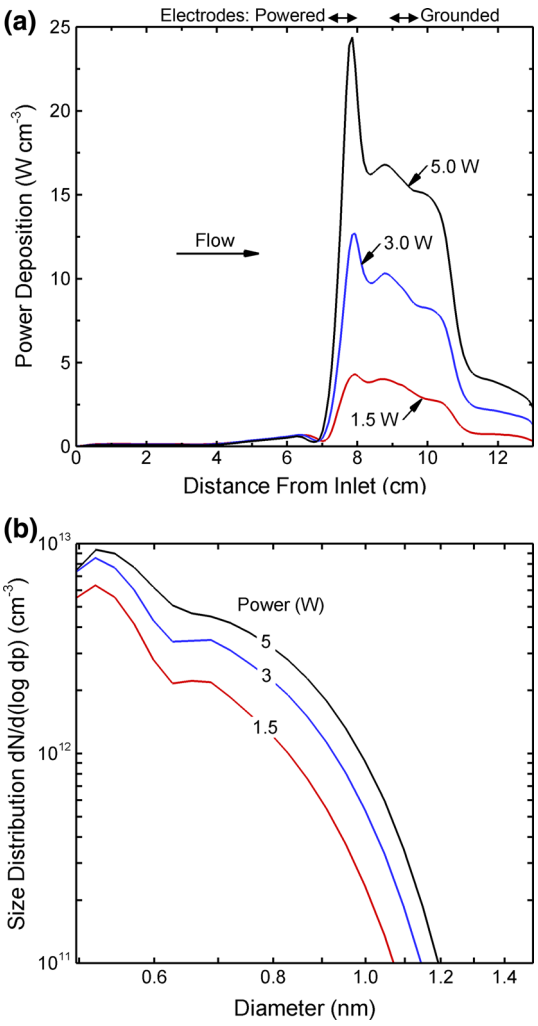

Fig. 13 Plasma properties for different power deposition for otherwise the base case conditions. **a** Power density on axis for 1.5, 3, and 5 W. **b** Particle size distribution at 2 cm from the outlet along the centerline as a function of input power

temperature produced by the plasma transport model and the internal temperature for 2-nm-diameter particles are shown in Fig. 12. The gas temperature is the mole-fraction-weighted average of the individual temperatures of neutral argon, helium, and silicon hydride species. The gas temperature peaks between the electrodes, at 440–450 K, where ion densities are largest, as the major source of gas heating is charge exchange with the hotter ions. Although the gas temperature exceeds ambient by as much as 100 K (the wall temperature is 325 K), the gas temperature remains well below the required crystallization temperature. These results are consistent with temperatures reported in experiments [15]. We found that the average internal temperature of 2-nm particles peaks between the two electrodes at 866 K. The contribution of ion-recombination on the surface of particles to the internal temperature is larger than heating by hydrogen surface reactions by a factor of 5. Similar modeling by Kramer et al. [48] showed that the contribution of hydrogen reactions increases with nanoparticle size, because conditions that produce larger particles also generally produce larger H atom densities relative to ion densities. For 3-nm-diameter

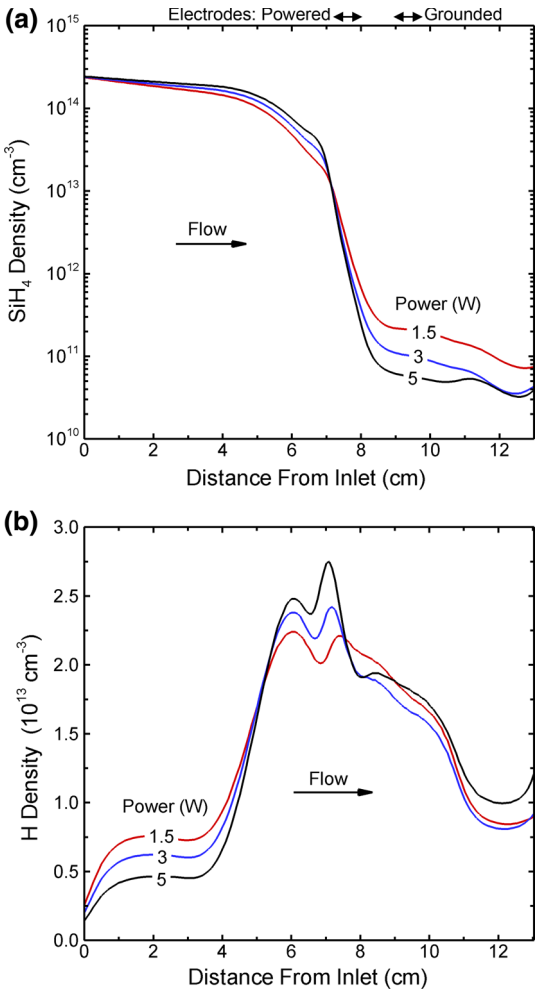

Fig. 14 The densities of **a** SiH_4 and **b** H for power deposition of 1.5, 3, and 5 W

particles, they found that both mechanisms have similar contributions. In this work, the Ar^+ density (10^{12} cm^{-3}) is about an order of magnitude larger than indicated by electrostatic capacitive probe measurements, while the hydrogen density is comparable. These differences in ion densities likely explain the larger contribution to internal temperature in our work due to ion recombination than predicted by Kramer et al. The predicted internal temperature for 2-nm particles is more than 400 K higher than the gas temperature and exceeds the crystallization temperature. The results of the model therefore predict the possibility of synthesizing crystalline silicon nanoparticles under these conditions.

Scaling with Power

Power deposition impacts nanoparticle synthesis from multiple perspectives. Higher power likely produces higher rates of dissociation of feedstock gases which increases particle growth rates. Higher ion densities and H atom densities with higher power likely produce higher internal particle temperatures, which leads to more crystallization [48]. Power densities are shown in Fig. 13a along the centerline of the reactor for total powers of 1.5, 3 and 5 W. The distribution of nanoparticle sizes at the outlet on the centerline is shown in Fig. 13b for all powers. Peak power deposition increases from 4 W cm^{-3} for 1.5 W power input to 24 W cm^{-3} for 5 W. Due to the higher production of radicals at higher power, particles grow to larger size and have higher total density. The densities of SiH_4 and H along the centerline are shown in Fig. 14 for powers from 1.5 to 5 W. For all powers, SiH_4 is essentially fully dissociated, and so its density between the electrodes where nucleation is maximum does not vary significantly from 1.5 to 5 W. SiH_4 is the source for H atoms, and since SiH_4 is nearly fully dissociated for all powers, the H density does not increase significantly with power. Nanoparticle temperature, and argon ion and hydrogen densities are shown in Fig. 15. The Ar^+ density increases nearly linearly with power while the H density remains fairly constant due to the nearly complete dissociation of SiH_4. With nanoparticle heating being mainly due to ion recombination on nanoparticle surfaces for these conditions, the nanoparticle temperature scales with the argon ion density.

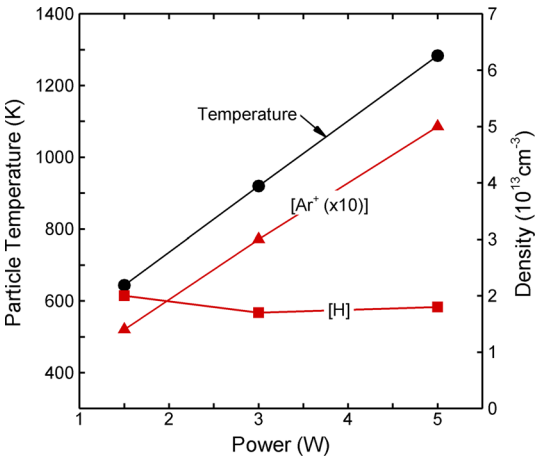

Fig. 15 Particle temperature calculated from Monte Carlo simulations, and hydrogen and argon ion densities as function of power deposition. Results are at 4 cm from the outlet along the centerline where the particle temperature peaks

Concluding Remarks

In this investigation, we developed a two-dimensional numerical model of a capacitively-coupled RF plasma as used for the synthesis of silicon nanoparticles. A sectional model was used to self-consistently calculate rates of nucleation and radical deposition on the surfaces of the nanoparticles. Coagulation processes were included with algorithms for the distribution of the nanoparticle charge and transport.

We found that silane dissociation occurs dominantly by hydrogen abstraction above the electrode, and electron impact reactions around and below the powered electrode. The predominant anion for initiating nanoparticle nucleation was found to be $Si_2H_5^-$ reacting with disilane, the latter of which is produced by insertion of SiH_2 in SiH_4. The greatest contribution to surface growth is neutral radicals since the majority of nanoparticles are negatively charged, which precludes anion–anion interactions. Coagulation is a significant growth mechanism due to the relatively high proportion of neutral nanoparticles.

Electron temperatures are sufficiently high (3.5 eV) throughout the discharge to produce nanoparticles that are dominantly negatively charged. The wall potential is lower than the plasma potential which radially traps negative particles, further increasing their density on the centerline compared to neutral nanoparticles, which can diffuse radially. However, the negative particles are not trapped in the axial direction. The model predicts that internal nanoparticle temperatures can be few hundred Kelvin greater than the gas temperature and commensurate with or above nanoparticle crystallization temperatures.

The modeling approach used in this investigation is intended to address system level issues (e.g., dependence of particle size on power, geometry, flow rate) while being less rigorous at addressing atomic level properties, such as the morphology of the particles. Computational techniques such as molecular dynamics are able to address these atomic level properties in the formation of silicon nanoparticles having as many as 20 Si atoms [53] while perhaps not being as rigorous at representing system level properties. These two approaches are quite symbiotic. The system level modeling requires the fundamental rate coefficients and thermodynamic properties that result from atomistic simulations. At the same time, realistic initial conditions are best used for the atomistic calculations, and these conditions can be provided by system level models.

Acknowledgments We thank P. Seal and D. G. Truhlar for providing their calculations of the Gibbs free energy changes reported in Table 3. This work was supported by the U.S. National Science Foundation (CHE-124752) and the U.S. Dept. of Energy Office of Fusion Energy Science (DE-SC0001939).

References

1. Moore D, Krishnamurthy S, Chao Y, Wang Q, Brabazon D, McNally PJ (2011) Characteristics of silicon nanocrystals for photovoltaic applications. Phys Status Solidi 208(3):604–607
2. Weis S, Kormer R, Jank MPM, Lemberger M, Otto M, Ryssel H, Peukert W, Frey L (2011) Conduction mechanisms and environmental sensitivity of solution-processed silicon nanoparticle layers for thin-film transistors. Small 7(20):2853–2857
3. Fujioka K, Hiruoka M, Sato K, Manabe N, Miyasaka R, Hanada S, Hoshino A, Tilley RD, Manome Y, Hirakuri K, Yamamoto K (2008) Luminescent passive-oxidized silicon quantum dots as biological staining labels and their cytotoxicity effects at high concentration. Nanotechnology 19:1–7
4. Shirahata N (2011) Colloidal Si nanocrystals: a controlled organic–inorganic interface and its implications of color-tuning and chemical design toward sophisticated architectures. Phys Chem Chem Phys 13:7284–7294

5. Gao X, Cui Y, Levenson RM, Chung LWK, Nie S (2004) In vivo cancer targeting and imaging with semiconductor quantum dots. Nat Biotechnol 22(8):969–976
6. Astruc D, Lu F, Aranzaes JR (2005) Nanoparticles as recyclable catalysts: the frontier between homogeneous and heterogeneous catalysis. Angew Chem Int Ed 44(48):7852–7872
7. Doğan I, van de Sanden MCM (2015) Gas-phase plasma synthesis of free-standing silicon nanoparticles for future energy applications. Plasma Process Polym 13(1):19–53
8. Littau K, Szajowski P (1993) A luminescent silicon nanocrystal colloid via a high-temperature aerosol reaction. J Phys Chem 97:1224–1230
9. Huisken F, Amans D, Ledoux G, Hofmeister H, Cichos F, Martin J (2003) Nanostructuration with visible-light-emitting silicon nanocrystals. New J Phys 5(1):10
10. Kortshagen U (2009) Nonthermal plasma synthesis of semiconductor nanocrystals. J Phys D Appl Phys 42(11):113001
11. Mangolini L, Thimsen E, Kortshagen U (2005) High-yield plasma synthesis of luminescent silicon nanocrystals. Nano Lett 5(4):655–659
12. Sankaran RM, Holunga D, Flagan RC, Giapis KP (2005) Synthesis of blue luminescent Si nanoparticles using atmospheric-pressure microdischarges. Nano Lett 5(3):537–541
13. Lopez T, Mangolini L (2014) On the nucleation and crystallization of nanoparticles in continuous-flow nonthermal plasma reactors. J Vac Sci Technol B Nanotechnol Microelectron Mater Process Meas Phenom 32(6):061802
14. Askari S, Levchenko I, Ostrikov K, Maguire P, Mariotti D (2014) Crystalline Si nanoparticles below crystallization threshold: effects of collisional heating in non-thermal atmospheric-pressure microplasmas. Appl Phys Lett 104(16):163103
15. Hirasawa M, Orii T, Seto T (2006) Size-dependent crystallization of Si nanoparticles. Appl Phys Lett 88(9):2004–2007
16. Mangolini L, Kortshagen U (2009) Selective nanoparticle heating: another form of nonequilibrium in dusty plasmas. Phys Rev E 79(2):026405
17. Boufendi L, Bouchoule A (1994) Particle nucleation and growth in a low-pressure argon-silane discharge. Plasma Sources Sci Technol 3(3):262–267
18. Boufendi L (1996) Electrical characterization and modeling of a dust forming plasma in a radio frequency discharge. J Vac Sci Technol A Vac Surf Film 14(2):572
19. Bilik N, Anthony R, Merritt BA, Aydil ES, Kortshagen UR (2015) Langmuir probe measurements of electron energy probability functions in dusty plasmas. J Phys D Appl Phys 48(10):105204
20. Denysenko I, Yu MY, Ostrikov K, Azarenkov NA, Stenflo L (2004) A kinetic model for an argon plasma containing dust grains. Phys Plasmas 11(11):4959
21. Denysenko I, Yu MY, Ostrikov K, Smolyakov A (2004) Spatially averaged model of complex-plasma discharge with self-consistent electron energy distribution. Phys Rev E 70(4):046403
22. Denysenko I, Ostrikov K, Yu MY, Azarenkov NA (2006) Behavior of the electron temperature in nonuniform complex plasmas. Phys Rev E 74(3):036402
23. Bhandarkar UV, Swihart MT, Girshick SL, Kortshagen UR (2000) Modelling of silicon hydride clustering in a low-pressure silane plasma. J Phys D Appl Phys 33(21):2731–2746
24. Bhandarkar U, Kortshagen U, Girshick SL (2003) Numerical study of the effect of gas temperature on the time for onset of particle nucleation in argon–silane low-pressure plasmas. J Phys D Appl Phys 36(12):1399–1408
25. Bao JL, Seal P, Truhlar DG (2015) Nanodusty plasma chemistry: a mechanistic and variational transition state theory study of the initial steps of silyl anion–silane and silylene anion–silane polymerization reactions. Phys Chem Chem Phys 17(24):15928–15935
26. Matsoukas T, Russell M (1995) Particle charging in low-pressure plasmas. J Appl Phys 77(1995):4285–4292
27. Cui C, Goree J (1994) Fluctuations of the charge on a dust grain in a plasma. IEEE Trans Plasma Sci 22(2):151–158
28. Le Picard R, Girshick SL (2016) The effect of single-particle charge limits on charge distributions in dusty plasmas. J Phys D Appl Phys 49:095201
29. Warthesen SJ, Girshick SL (2007) Numerical simulation of the spatiotemporal evolution of a nanoparticle–plasma system. Plasma Chem Plasma Process 27(3):292–310
30. Agarwal P, Girshick SL (2012) Sectional modeling of nanoparticle size and charge distributions in dusty plasmas. Plasma Sources Sci Technol 21(5):055023
31. Ravi L, Girshick SL (2009) Coagulation of nanoparticles in a plasma. Phys Rev E 79(2):026408
32. Gresback R, Holman Z, Kortshagen U (2007) Nonthermal plasma synthesis of size-controlled, monodisperse, freestanding germanium nanocrystals. Appl Phys Lett 91(9):093119

33. Kramer NJ, Schramke KS, Kortshagen UR (2015) Plasmonic properties of silicon nanocrystals doped with boron and phosphorus. Nano Lett 15(8):5597–5603
34. Kushner MJ (2009) Hybrid modelling of low temperature plasmas for fundamental investigations and equipment design. J Phys D Appl Phys 42(19):194013
35. Gelbard F, Tambour Y, Seinfeld JH (1980) Sectional representations for simulating aerosol dynamics. J Colloid Interface Sci 76(2):541–556
36. Wu C-Y, Biswas P (1998) Study of numerical diffusion in a discrete-sectional model and its application to aerosol dynamics simulation. Aerosol Sci Technol 29(5):359–378
37. Draine BT, Sutin B (1987) Collisional charging of interstellar grains. Astrophys J 320:803–817
38. Barnes MS, Keller JH, Forster JC, O'Neill JA, Coultas DK (1992) Transport of dust particles in glow-discharge plasmas. Phys Rev Lett 68(3):313
39. Huang DD, Seinfeld JH, Okuyama K (1991) Image potential between a charged particle and an uncharged particle in aerosol coagulation—enhancement in all size regimes and interplay with van der Waals forces. J Colloid Interface Sci 141(1):191–198
40. Perrin J, Schmitt JP, De Rosny G, Drevillon B, Huc J, Lloret A (1982) Dissociation cross sections of silane and disilane by electron impact. Chem Phys 73:383–394
41. Buss RJ, Ho P, Weber ME (1993) Laser studies of the reactivity of SiO with the surface of a depositing film. Plasma Chem Plasma Process 13(1):61–76
42. Hawa T, Zachariah MR (2005) Coalescence kinetics of bare and hydrogen-coated silicon nanoparticles: a molecular dynamics study. Phys Rev B Condens Matter Mater Phys 71(16):1–12
43. Allen JE (1992) Probe theory—the orbital motion approach. Phys Scr 45(5):497–503
44. Dagum L, Menon R (1998) OpenMP: an industry-standard API for shared-memory programming. Comput Sci Eng IEEE 5(1):46–55
45. Seal P, Truhlar DG (2014) Large entropic effects on the thermochemistry of silicon nanodusty plasma constituents. J Am Chem Soc 136(7):2786–2799
46. Yavneh I (1996) On red-black SOR smoothing in multigrid. SIAM J Sci Comput 17(1):180–192
47. LaRowe RP, Ellis CS (1991) Page placement policies for NUMA multiprocessors. J Parallel Distrib Comput 11(2):112–129
48. Kramer NJ, Anthony RJ, Mamunuru M, Aydil ES, Kortshagen UR (2014) Plasma-induced crystallization of silicon nanoparticles. J Phys D Appl Phys 47(7):075202
49. Matsoukas T (1994) Charge distributions in bipolar particle charging. J Aerosol Sci 25(4):599–609
50. Tawara H, Itikawa Y, Nishimura H, Yoshino M (1990) Cross sections and related data for electron collisions with hydrogen molecules and molecular ions. J Phys Chem Ref Data 19(3):617–633
51. Agarwal P, Girshick SL (2014) Numerical modeling of the spatiotemporal behavior of an RF argon-silane plasma with dust particle nucleation and growth. Plasma Chem Plasma Process 34(3):489–503
52. Maurer HR, Kersten H (2011) On the heating of nano- and microparticles in process plasmas. J Phys D Appl Phys 44(17):174029
53. Forero-Martinez NC, Le Thi H-L, Vach H (2014) Self-assembly in silane/hydrogen plasmas: from silicon atoms to aromatic silicon nanocrystals. Plasma Chem Plasma Proc 34:535–543